Acta Materialia 213 (2021) 116964

Contents lists available at ScienceDirect

Acta Materialia

journal homepage: www.elsevier.com/locate/actamat

Dislocation electron tomography: A technique to characterize the dislocation microstructure evolution in zirconium alloys under irradiation

Alexandre Mussi[a,*], Ahmed Addad[a], Fabien Onimus[b]

[a] Univ. Lille, CNRS, INRAE, Centrale Lille, UMR 8207 - UMET - Unité Matériaux et Transformations, F-59000 Lille, France
[b] Université Paris-Saclay, CEA, Service de Recherches Métallurgiques Appliquées, Gif-sur-Yvette 91191, France

ARTICLE INFO

Article history:
Received 22 September 2020
Revised 15 March 2021
Accepted 2 May 2021
Available online 9 May 2021

Keywords:
Dislocation
Tomography
Irradiation
Helix
Loops

ABSTRACT

Diffraction-contrast electron tomography was used to analyse the 3D geometry of the dislocation microstructure in a zirconium alloy before and after ion irradiation. The material had been strained at room temperature prior to irradiation. After straining, the material exhibited mainly screw dislocations with <a> Burgers vectors. From the analysis of the habit plane of <a> dislocations with non-screw segments, it was deduced that they have glided mainly in the prismatic planes and to a lesser extent in the first order pyramidal planes. After irradiation, dislocation loops with <a> Burgers vectors were observed. It was shown that the loops are not pure edge and have their habit plane located around the planes $\{10\bar{1}0\}$, tilted up to 20° towards the planes (0001) and $\{11\bar{2}0\}$. Furthermore, it was proven that the initial screw dislocations have climbed under irradiation. Several dislocations were also found to have interacted with loops during climb. The climb of <a> dislocations under irradiation is an important mechanism that can explain part of the in-reactor deformation of zirconium alloys when subjected to simultaneous mechanical loading and irradiation. Interactions between dislocations and loops occurring during dislocation climb may also play a significant role on the in-reactor deformation of zirconium alloys.

1. Introduction

Cladding tubes and structure components made of zirconium alloys, which are used for light and heavy water nuclear reactors, exhibit in-reactor deformation during normal operation [1,2]. The in-reactor deformation of zirconium alloys is mainly the result of two phenomena: irradiation induced growth and irradiation creep [3–5]. Irradiation creep deformation occurs when the material undergoes simultaneous mechanical loading and neutron irradiation [6,7], whereas irradiation induced growth occurs without any applied load [8]. Several mechanisms have been proposed in the literature to explain the irradiation creep phenomenon [9,5]. Most of these deformation mechanisms are based on dislocation climb, or climb and glide, under irradiation [10–17]. Dislocation climb under irradiation is a well-acknowledged mechanism from a theoretical point of view, but there is little experimental evidence of this phenomenon in the case of zirconium alloys. In order to gain more evidence of this mechanism, an experimental study has been undertaken. In this work, dislocation climb under irradiation is analysed, but without any applied stress.

Dislocation climb has been observed after quenching a Zr-1%Al alloy. In that case, helical dislocations were clearly observed [18]. Under irradiation, there have been only a few observations of dislocation climb in zirconium alloys. In the case of dislocations with <a> Burgers vector, Buckley and Manthorpe [19] showed a picture of helical climb of <a> dislocations at 500°C under 1 MeV electron irradiation. Griffiths [20] reported observations of dislocation climb under 1 MeV electron irradiation at 402°C. Recently, Gaumé et al. [21] have also conducted the same type of experiments. They observed helical climb of <a> dislocations under 1 MeV electron irradiation at 450°C. The magnitude of dislocation climb remained limited under electron irradiation. However, when analysing the microstructure after Zr ion irradiation conducted at 450°C, they observed wavy dislocations. They hypothesized that the wavy shape of the dislocations was the result of dislocation climb under irradiation.

* Corresponding author at: Université Lille, Unité Matériaux Et Transformations - UMR CNRS 8207, Villeneuve d'Ascq Cedex 59655, France.
E-mail address: alexandre.mussi@univ-lille.fr (A. Mussi).

https://doi.org/10.1016/j.actamat.2021.116964

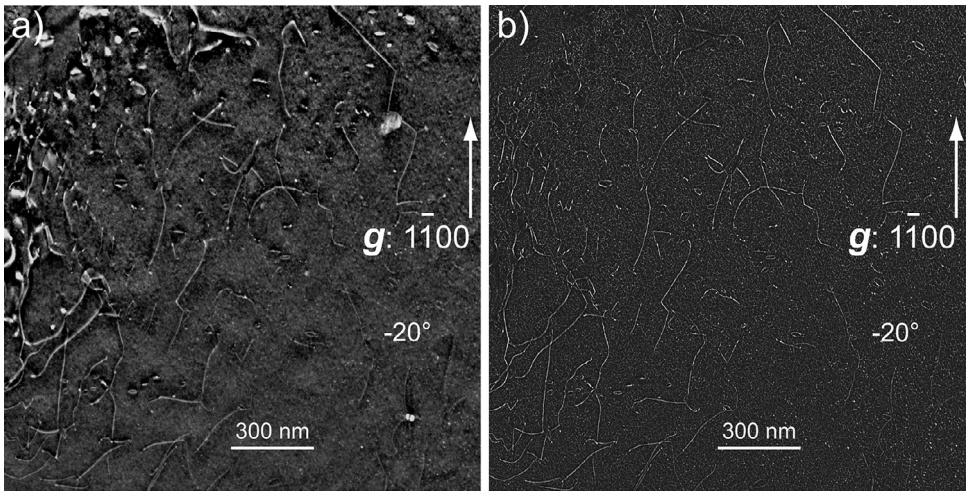

Fig. 1. Numerical filtering method to enhance the dislocation contrast: (a) raw WBDF-STEM contrast of dislocation (the background and dislocation contrasts are not homogeneous); (b) Fig. 1a numerically filtered using the "Rolling ball radius" option of the "Subtract Background" tool of the ImageJ software (the background and dislocation contrasts are now homogeneous).

Table 1
Chemical composition (wt. %) of the recrystallized Zircaloy-4 thin sheet used in this study.

Sn	Fe	Cr	O	Zr
1.32	0.215	0.108	0.125	bal.

In order to gain a better understanding of the tri-dimensional geometry of these dislocations, and to characterize the dislocation climb under irradiation in greater detail, an advanced technique, called Dislocation Electron Tomography (DET), using diffraction-contrast electron tomography in a TEM [22–25], has been used. It must be noted that this technique has also recently been used by Feng et al. [26] to study dislocation helices created by dislocation climb in a quenched Al-Cu-Mg alloy.

In the first part of this paper, the material and experimental details are described. Then the diffraction-contrast electron tomography technique is presented along with the data post-processing method. The results are then presented and discussed.

2. Material and experimental details

The material used for this study is a cold-rolled thin sheet of Zircaloy-4 in the recrystallized metallurgical state, which is often considered as a model material for recrystallized zirconium alloys. The chemical composition of this alloy is given in Table 1.

In the as-received state, this material exhibits a microstructure made of equi-axed grains with an average diameter of 6 µm, containing only few dislocations (typically 10^{11} m^{-2}). This material also exhibits a crystallographic texture typical of recrystallized zirconium alloy thin rolled sheet. The majority of the grains are oriented such that the <c> axis of the hexagonal close-packed (hcp) lattice of the grain is in the plane ND-TD (ND: Normal Direction, TD: Transverse Direction) and tilted up to 20° away from ND [27,28].

2.1. Preparation of the non-irradiated strained sample

In order to analyze the dislocation climb mechanism under irradiation, the cold-rolled sheet was strained up to an additional 1% plastic strain in the rolling direction, at room temperature, prior to irradiation, to increase the dislocation density. During the plastic deformation, <a> dislocations were created, leading to a microstructure containing a significant amount of dislocations (typically 10^{13} m^{-2}). These dislocations are homogeneously distributed throughout the grains that are well oriented for <a> slip. Because of the texture of the material, these grains represent the majority of grains in the material. After straining, samples were first mechanically polished, and 3 mm diameter disks were punched out. One of these disks was jet electropolished on both sides using an electrolytic solution of 90% ethanol and 10% perchloric acid at -10°C, then analyzed by diffraction-contrast electron tomography.

2.2. Preparation of the irradiated strained sample

Another sample was first jet electropolished on one side only and then irradiated on the ARAMIS-facility at CSNSM/IN2P3 Orsay using 600 keV Zr^{+} ions at 450°C. The fluence was 8×10^{17} ions.m^{-2}, which corresponds to an average dose of 0.27 dpa over the thin foil of thickness 150 nm. This value was calculated using the software called SRIM [29,30], which computes the number of atoms displaced by energetic particles using a Monte-Carlo approach. A displacement threshold energy of 40 eV was chosen, and the "quick calculation of damage" mode was used. During the experiments, the damage rate was about 5×10^{-5} dpa.s^{-1}. It can be noted that using the "full damage cascade" mode, the SRIM software computes a dose of 0.5 dpa.

After irradiation, the irradiated surface was protected by a lacquer, and the sample was electropolished on the opposite face to create a hole surrounded by a thin area suitable for TEM analysis. Because the irradiated layer was 300 nm thick, the entire observable area, which had a thickness of 100 to 200 nm, was fully irradiated.

2.3. First TEM analyses of the irradiated strained specimen

The thin foil was first observed using a conventional TEM method. After irradiation, dislocation loops with <a> Burgers vector have been observed. These loops had a mean diameter of 32 nm with a number density of 6×10^{20} m^{-3}. All of the loops analysed have been found to be of interstitial nature [21]. The fact that only interstitial loops were observed may be explained by the presence of a free surface during the irradiation, which could act as sink (unbiased sink) for vacancies. It is nevertheless worth pointing out that the microstructural evolution of zirconium alloys under irradiation is still not fully understood. Wavy dislocations

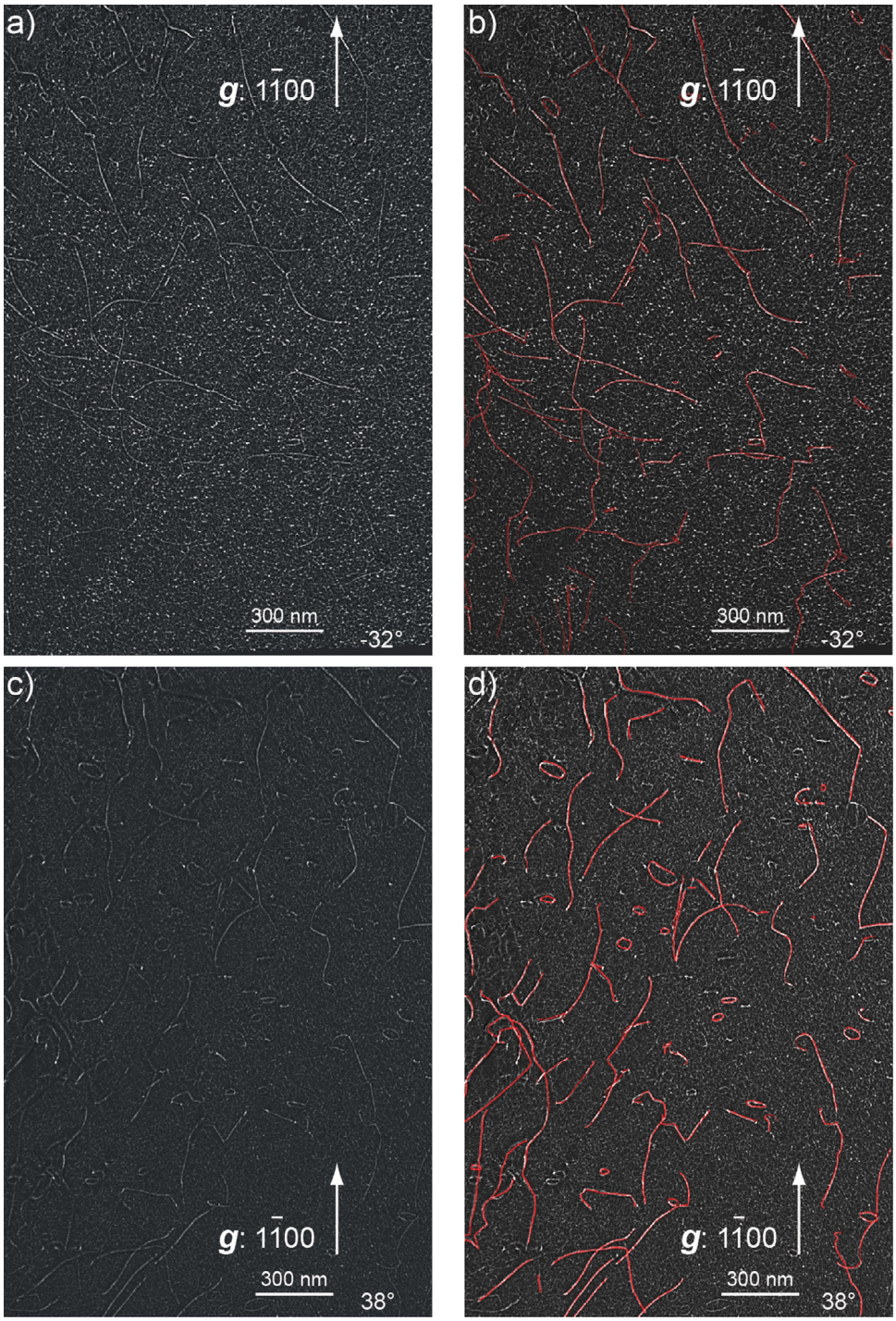

Fig. 2. Tomographic reconstruction of the irradiated Zr specimen obtained with the 1$\bar{1}$00 diffraction vector: (a) micrograph in WBDF-STEM mode (numerically filtered) with a projection angle of -32°; (b) superimposition on Fig. 2a of the tomographic reconstruction (redrawn with the UCSF Chimera) for the same projection angle; (c) micrograph in WBDF-STEM mode (numerically filtered) with a projection angle of 38°; (d) superimposition on Fig. 2c of the tomographic reconstruction (redrawn with the UCSF Chimera) for the same projection angle. Movie versions of the numerically filtered tilted series, the redrawn volume and the superimposition redrawn volume on the tilted series are shown in Supplemental file S1, S2 and S3.

were also observed after irradiation, probably resulting from helical climb under irradiation.

3. Dislocation electron tomography and post-processing method

DET is a tomographic technique developed for TEM, based on conventional diffraction contrast imaging of dislocations. The principle of this method is to perfectly align a diffraction vector, used to observe dislocations, along the tilt axis. Then, by taking several pictures of the sample for various tilt angles, the 3D dislocation microstructure can be obtained. Contrary to the classical stereographic projection method, DET provides a large amount of information that can be used for statistical and quantitative studies [31]. Two analyses were performed: a conventional tomographic

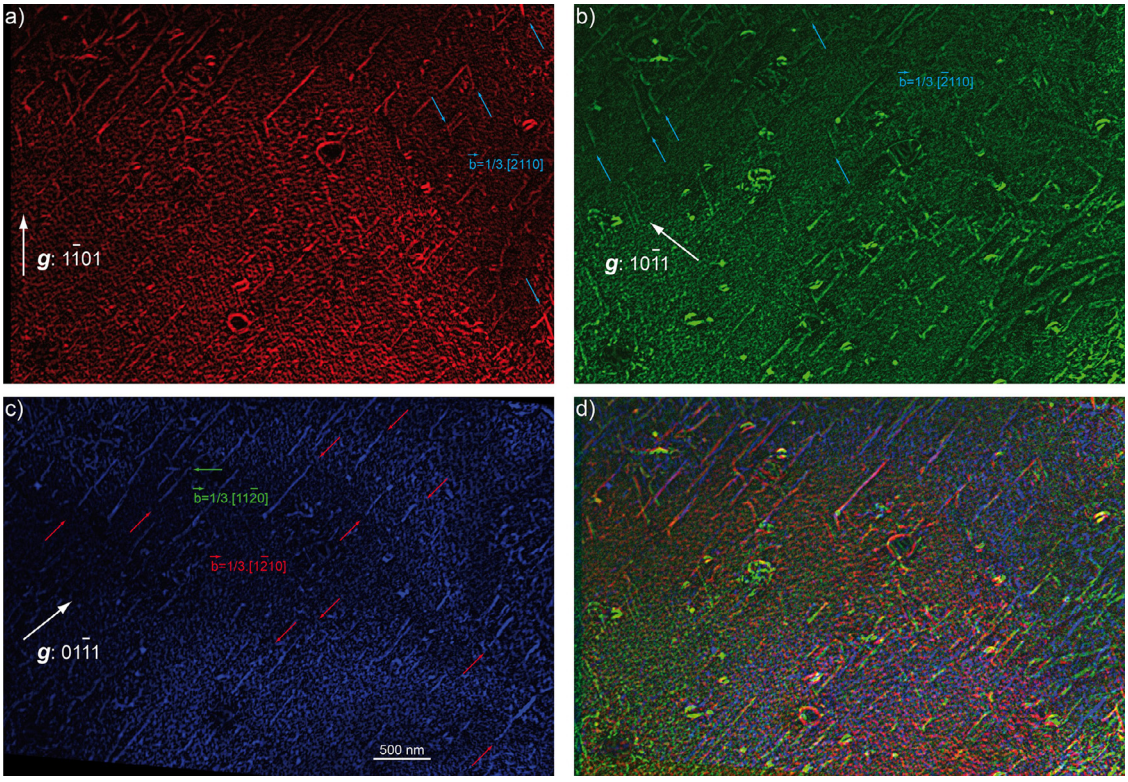

Fig. 3. Burgers vector indexations of the non-irradiated Zr specimen: (a) micrograph in WBDF-TEM mode obtained with the $1\bar{1}01$ diffraction vector, dislocations with $\pm 1/3[1\bar{2}10]$ and $\pm 1/3[\bar{2}110]$ Burgers vectors are in contrast; (b) micrograph obtained with *g*: $1\bar{1}01$, dislocations with $\pm 1/3[\bar{2}110]$ and $\pm 1/3[11\bar{2}0]$ Burgers vectors are in contrast; (c) micrograph obtained with *g*: $01\bar{1}1$, dislocations with $\pm 1/3[11\bar{2}0]$ and $\pm 1/3[1\bar{2}10]$ Burgers vectors are in contrast; (d) superimposition of the previous micrographs to facilitate Burgers vector indexations. Dislocations with $\pm 1/3[1\bar{2}10]$, $\pm 1/3[\bar{2}110]$ and $\pm 1/3[11\bar{2}0]$ Burgers vectors are pointed out by red, blue and green arrows respectively. Dislocations are highly straight-lined with a strong screw nature (very few dislocations with a $\pm 1/3[11\bar{2}0]$ Burgers vector are observed). Movie versions of the raw tilted series, the redrawn volume and the superimposition redrawn volume on the tilted series are shown in Supplemental file S4, S5 and S6.(For interpretation of the references to color in this figure legend, the reader is referred to the web version of this article.).

characterization and a high-spatial-resolution tomographic characterization.

3.1. Conventional dislocation electron tomography

The conventional DET analysis was performed on the non-irradiated Zircaloy-4 specimen using a FEI® Tecnaï $G^2$20 Twin microscope, operating at 200 kV with a LaB_6 filament. The tilt-series required to perform the tomographic reconstruction was obtained using a double-tilt sample-holder with an angular range of ±60°. The diffraction vector was oriented parallel to the sample-holder's main axis (the $1\bar{1}01$ diffraction vector was used for this tilt-series). Dislocation micrographs were acquired every 5° from -60° to 50° with the weak-beam dark-field (WBDF) TEM mode. With these acquisition conditions, the signal to noise ratio was high. The major disadvantage of the TEM-WBDF mode is the contrast heterogeneity resulting from thickness fringes and bend-contours that disturb the background contrast. On the other hand, the scanning transmission electron microscope (STEM) mode can produce homogeneous background and dislocation contrasts [32,33], but the signal to noise ratio is weak when using a LaB_6 filament [34]. To get a homogeneous contrast while maintaining a high signal to noise ratio, we decided to use a precessing electron beam [35], which integrates the relrod rocking-curves in the reciprocal space and averages the background and dislocation contrasts. In addition, the greater the precession angle, the larger the homogeneous contrast domain. A precession angle of 0.3° enabled us to achieve a homogeneous contrast over approximately 6 μm in diameter, thus leading to a more statistical study of the 3D dislocation microstructure. To ensure that the objective aperture did not hide the precessed electron beam, an intermediate aperture size of 50 μm was used. The spatial resolution of the reconstructed images is degraded by the precession, due to the slight misorientation of the diffraction vector from the sample-holder main axis but also by the tomographic reconstruction interpolations.

3.2. High-resolution dislocation electron tomography

The high resolution DET was obtained on the irradiated Zircaloy-4 specimen using a ThermoFisher® Titan Themis microscope, operating at 300 kV with a X-FEG filament. As STEM and conventional TEM imaging techniques are equivalent through the principle of reciprocity [32,33], the STEM mode was employed since the X-FEG gun is bright enough to generate dislocation micrographs with a high signal to noise ratio despite the high Bragg deviation parameter (essential for optimizing the dislocation thickness spatial resolution) associated with a homogeneous contrast. The tilt-series has been acquired with the High Angle Triple Axes (HATA) sample-holder dedicated to DET [36]. This sample-holder gives access to angular ranges of ±80° for α, ±7.5° for β and ±2.5° for Ω with an accuracy of approximately 0.1° considering the backlash. This sample holder made it possible to accurately orientate the diffraction vector along the sample-holder's main axis (the $1\bar{1}00$ diffraction vector was chosen for this tilt-series). In order to limit interpolation and extrapolation errors during the tomographic reconstruction, images were acquired every 2° from -60° to 68°. To obtain diffraction contrasts where only (nñ00) plane families were involved, the electron beam was tilted to align the ($1\bar{1}00$) and ($2\bar{2}00$) diffraction discs (slightly superimposed) on the bright field detector. Then, the HATA sample-holder was tilted

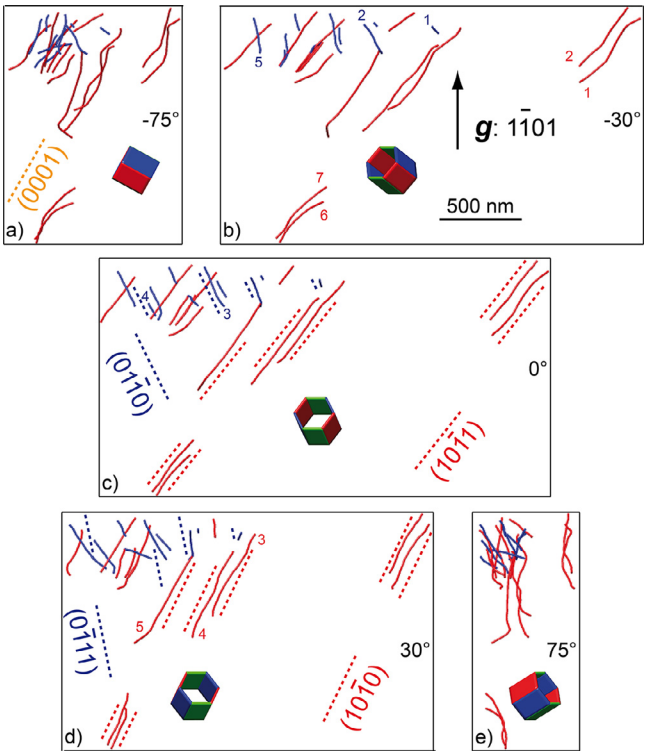

Fig. 4. Glide plane characterization of the non-irradiated Zr specimen ($\pm 1/3[1\bar{2}10]$ Burgers vectors colored in red and $\pm 1/3[\bar{2}110]$ Burgers vectors colored in blue): (a) tomographic reconstruction, obtained with g: $1\bar{1}01$, for a -75° projection angle (the basal plane is edge-on in this orientation condition); (b) -30° projection angle; c) 0° projection angle ($(01\bar{1}0)$ and $(10\bar{1}1)$ are edge-on); d) 30° projection angle ($(0\bar{1}11)$ and $(10\bar{1}0)$ are edge-on); e) 75° projection angle. 7 red dislocations and 5 blue dislocations are pointed out. (For interpretation of the references to color in this figure legend, the reader is referred to the web version of this article.).

along the angle β to be in STEM-WBDF conditions in order to distinguish the smallest details of the dislocations without losing contrast.

3.3. Post-processing method

We undertook a manual alignment with one-pixel accuracy for the irradiated Zircaloy-4 specimen tilt-series (accuracy details are provided in Supplementary Material) and with an average precision for the non-irradiated specimen tilt-series. Then, the tomographic reconstruction inaccuracies of the non-irradiated Zircaloy-4 specimen low-resolution tilt-series (composed of only 23 micrographs) were reduced by redrawing by hand the dislocations of each micrograph to obtain a black and white contrast. Concerning the high-resolution tilt-series of the irradiated Zircaloy-4 specimen (composed of 65 micrographs), since the quality of the micrographs was high, it was considered that a simple numerical filter (background subtraction with the free ImageJ software) was sufficient to enhance the dislocation contrast (Fig. 1). Both reconstructions were performed using the Weighted Back Projection (WBP) algorithm [37]. This algorithm, which is based on the Radon transformation [38], is freely available from the TomoJ plugin [39] of the ImageJ software. Despite a variety of precautions, tomographic reconstructions are not perfect. The highest inaccuracies are in the missing wedge (angular range where micrographs cannot be acquired), where the WBP algorithm performs extrapolations. Consequently, the measurement uncertainties of the dislocation positions are higher near projection angles of 90°, which arbitrarily thickens dislocation widths. Dislocation geometries are no longer cylindrical but exhibit ribbon shapes. We used the free UCSF Chimera software [40] to directly redraw dislocations into the volume [24,31,41] and regain the cylindrical dislocation geometries. To ensure dislocation tracking quality, we superimposed the redrawn volume on real micrographs (Fig. 2), allowing careful comparisons. When the projected redrawn volume was not in satisfactory agreement with real micrographs, the considered dislocation was discarded. Finally, each dislocation loop habit plane, or dislocation line habit plane, was indexed by tilting the reconstructed volume and the tilt-series during post-processing. When the projected dislocation loop, or line, is rectilinear, its habit plane is edge-on and can be indexed, as the crystal orientation is known. Back and forth cross-checks have to be done between reconstructed volumes and tilt-series to guarantee indexation accuracy (several habit planes were not indexed when doubts persisted between projections of the reconstructed volumes and tilt-series). Furthermore, the smallest loops (less than 8 nm in diameter) were not considered since they exhibit high indexation uncertainties.

4. Results

4.1. Non-irradiated Zircaloy-4 specimen

The WBDF micrographs of the non-irradiated Zircaloy-4 specimen, shown in Fig. 3, show mainly dislocations with straight line geometries. In order to characterize the dislocation Burgers vectors of this specimen, the extinction criterion technique was used. Dislocations with $\pm 1/3[1\bar{2}10]$ Burgers vectors (indicated with red arrows on Fig. 3c) and $\pm 1/3[\bar{2}110]$ Burgers vectors (indicated with blue arrows on Fig. 3a and b) are in contrast with the $1\bar{1}01$ diffraction vector (Fig. 3a). Dislocations with $\pm 1/3[\bar{2}110]$ Burgers vectors (blue arrows) and a single dislocation with a $\pm 1/3[11\bar{2}0]$ Burgers vector (indicated with a green arrow on Fig. 3c) are in contrast with the $10\bar{1}1$ diffraction vector (Fig. 3b). Finally, dislocations with $\pm 1/3[1\bar{2}10]$ Burgers vectors (red arrows) and the dislocation with a $\pm 1/3[11\bar{2}0]$ Burgers vector (green arrow) are in contrast with the $01\bar{1}1$ diffraction vector (Fig. 3c).

Except for one dislocation with Burgers vector $\pm 1/3[11\bar{2}0]$ (colored in green), most of the dislocations in the micrographs have a Burgers vectors of either $\underline{b} = \pm 1/3[1\bar{2}10]$ or $\underline{b} = \pm 1/3[\bar{2}110]$. In the reconstructed volume in Fig. 4, the dislocations with $\underline{b} = \pm 1/3[1\bar{2}10]$ are colored in red and the dislocations with $\underline{b} = \pm 1/3[\bar{2}110]$ are colored in blue.

It can be seen in Fig. 3 and in the reconstructed volume shown in Fig. 4, that the straight linear dislocations are aligned along their Burgers vector, showing that they are mainly screw dislocations. When part of the dislocation deviates from its Burgers vector orientation, the habit plane of the dislocation, which must be its glide plane, can be indexed. The glide planes of several dislocations were characterized using DET. Fig. 4 shows in detail the characterization of 7 "red" and 5 "blue" dislocations. Except for the blue dislocation n°2, which is essentially of screw nature, we determined the glide planes of the other blue dislocations, namely the $(01\bar{1}0)$ plane. The glide configuration for the red dislocations is more complex. As was the case for the blue dislocation n°2, the red dislocations n°2, 4 and 7 have too much screw nature, and we could not determine their glide plane. Dislocation n°5 clearly glides on the pyramidal $(10\bar{1}1)$ plane. Fig. 5 shows details of the glide plane indexation of the blue dislocation n°3 and the red dislocation n°5. The maximum deviations of dislocations from the screw nature were quantified when the normals to the glide planes were edge-on. In this condition, the angle α_2 between the dislocation line and the Burgers vector was measured. The highest deviation of the blue dislocation n°3 is $\alpha_2 \approx 33°$ and the highest deviation of the red dislocation n°5 is $\alpha_2 \approx 69°$. In these cases, the dislocations are sufficiently far from the screw orientation to be able to index their glide planes.

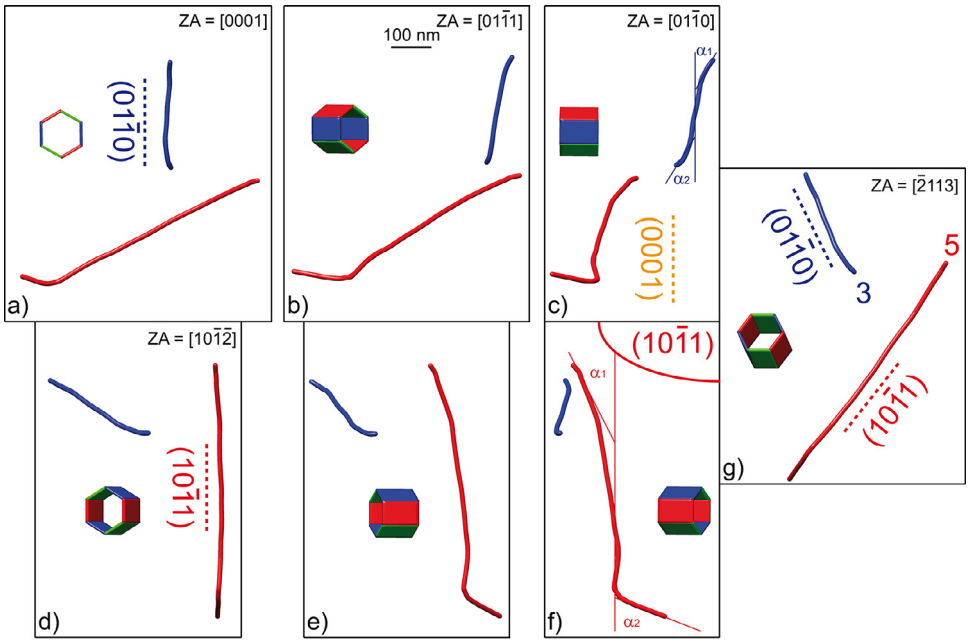

Fig. 5. Step back from the characterization of the blue dislocation n°3 and the red dislocation n°5: (a) tomographic reconstruction projection along [0001] ((01$\bar{1}$0) is edge-on); (b) intermediate projection (the (01$\bar{1}$0) plane is at 45° from the projection axis); (c) projection along [01$\bar{1}$0], the highest misorientation from the screw nature of the blue dislocation can be quantified (α_1 is the maximum deviation angle at the upper end of the dislocation and α_2 is the maximum deviation angle at the lower end of the dislocation); (d) projection along [10$\bar{1}\bar{2}$] ((10$\bar{1}$1) is edge-on); (e) intermediate projection (the (10$\bar{1}$1) plane is at 45° from the projection axis); (f) projection along the normal of (10$\bar{1}$1), the highest misorientation from the screw nature of the red dislocation can be quantified (α_1 is the maximum deviation angle at the upper end of the dislocation and α_2 is the maximum deviation angle at the lower end of the dislocation); (g) projection along [$\bar{2}$113] ((10$\bar{1}$1) and (01$\bar{1}$0) are edge-on). (For interpretation of the references to color in this figure legend, the reader is referred to the web version of this article.).

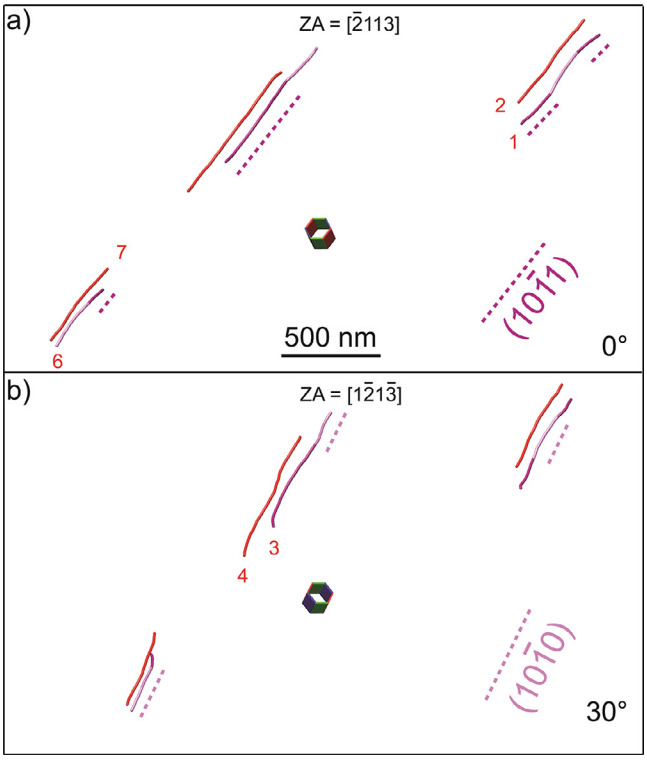

Fig. 6. Cross-slip: (a) tomographic reconstruction projection along the [$\bar{2}$113] direction (the (10$\bar{1}$1) glide plane is edge-on in this orientation condition); (b) tomographic reconstruction projection along the [1$\bar{2}$1$\bar{3}$] direction (the (10$\bar{1}$0) glide plane is edge-on in this orientation condition). It is worth noticing that dislocations 1, 3 and 6 are never totally straight-lined, suggesting that they have partly cross-slipped.

The projections of the red dislocation n°1, 3 and 6 are never entirely linear, whatever the orientation. This phenomenon could be explained by a cross-slip mechanism, of one part of the dislocation, from a prismatic plane to a first order pyramidal plane. Fig. 6 illustrates this mechanism for the red dislocations n°1, 3 and 6. It is precisely the $\pm 1/3[1\bar{2}10](10\bar{1}0)$ / $\pm 1/3[1\bar{2}10](10\bar{1}1)$ cross-slip mechanism. All of the indexed slip systems, cross-slip systems and dislocation screw configurations, are given in Table 2. To conclude, most of the dislocations have a screw nature. When the dislocations have sufficient deviation from the screw orientation and their glide planes can be indexed, we noticed that the $\{1\bar{1}00\}$ prismatic plane is predominant with few $\{1\bar{1}01\}$ pyramidal configurations, possibly due to the cross-slip mechanism.

4.2. Irradiated Zircaloy-4 specimen

The tomographic reconstruction of the irradiated Zr specimen, redrawn with the UCFS Chimera software [40], is shown in Fig. 7 for 5 projection angles (-75°, -30°, 0°, 30° and 75°). Dislocations are curved with 3D geometries. Numerous dislocation loops of a few dozen nm in diameter and also interactions between dislocation segments and loops are present in the 3D dislocation microstructure. The dislocations have lost nearly all of their screw nature. Only two screw dislocation segments with $\pm 1/3[1\bar{2}10]$ Burgers vectors (in red in Fig. 7, only screw dislocations are colored) and two screw dislocation segments with $\pm 1/3[\bar{2}110]$ Burgers vectors (in blue in Fig. 7, only screw dislocations are colored) remain.

Fig. 8 shows an example of Burgers vector indexations for five dislocation loops. Dislocation loops with $\pm 1/3[1\bar{2}10]$ and $\pm 1/3[\bar{2}110]$ Burgers vectors are in contrast with the $\bar{1}100$ diffraction vector (Fig. 8a); dislocation loops with $\pm 1/3[\bar{2}110]$ and $\pm 1/3[11\bar{2}0]$ Burgers vectors are in contrast with the $\bar{1}011$ diffraction vector (Fig. 8b); and dislocation loops with $\pm 1/3[1\bar{2}10]$ and $\pm 1/3[11\bar{2}0]$ Burgers vectors are in contrast with the $0\bar{1}11$ diffraction vector (Fig. 8c). We can conclude that the Burgers vector of

Table 2
Dislocation natures, slip systems and cross-slip systems for 29 dislocations observed in the non-irradiated Zr specimen.

Number of dislocations	Dislocation nature, Burgers vector, slip plans, cross-slip system
14	screw $\pm 1/3[1\bar{2}10]$
4	screw $\pm 1/3[\bar{2}110]$
1	mixed $\pm 1/3[1\bar{2}10](10\bar{1}0)$
6	mixed $\pm 1/3[\bar{2}110](01\bar{1}0)$
1	mixed $\pm 1/3[1\bar{2}10](10\bar{1}1)$
3	mixed $\pm 1/3[1\bar{2}10](10\bar{1}0)$ / $\pm 1/3[1\bar{2}10](10\bar{1}1)$

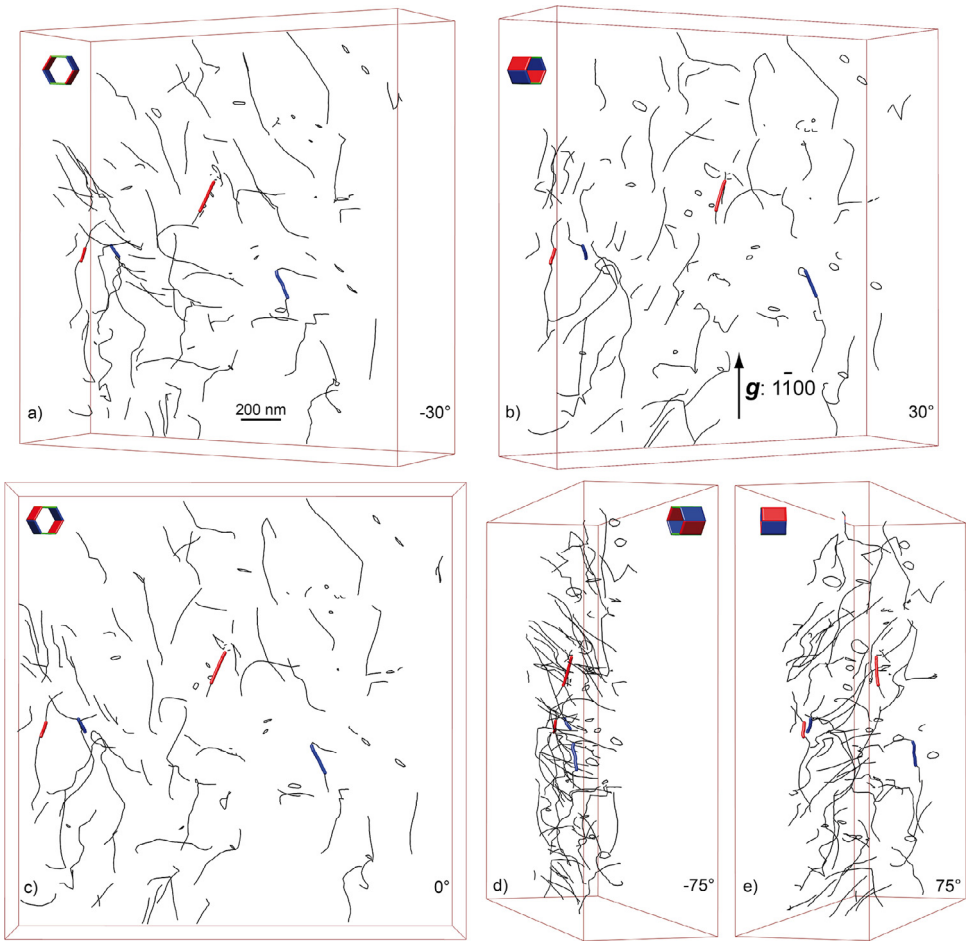

Fig. 7. 3D microstructure of the irradiated Zr specimen obtained with the $1\bar{1}00$ diffraction vector (the Burgers vectors of red screw dislocations are $\pm 1/3[1\bar{2}10]$ and the Burgers vectors of blue screw dislocations are $\pm 1/3[\bar{2}110]$). (a–e) Tomographic reconstruction oriented along the -75°, -30°, 0°, 30° and 75° projection angles. The 3D microstructure shows very few screw dislocation segments (only 2 blue and 2 red screw dislocation segments), numerous dislocation loops, wavy 3D dislocations and also interactions between dislocation segments and loops. (For interpretation of the references to color in this figure legend, the reader is referred to the web version of this article.).

dislocation loop n°4 (out of contrast on Fig. 8b and in contrast on Fig. 8a–c) is $\pm 1/3[1\bar{2}10]$ (number indicated in red on Fig. 8a, c–e, k); while the Burgers vector of the other dislocation loops (in contrast on Fig. 8a–c) is $\pm 1/3[\bar{2}110]$ (number indicated in blue on Fig. 8a, b, d, e, i, j, l and m). The 3D reconstruction of these five loops is illustrated in Fig. 8e–h with different projection angles (0°, 72°, 130° and 162° respectively). The habit plane of the loop n°3 is $(\bar{3}12\bar{2})$ (Fig. 8g) and the habit planes of loops n°1, 2, 4 and 5 are $(\bar{3}120)$, $(6\bar{5}\bar{1}1)$, $(01\bar{1}0)$ and $(10\bar{1}0)$ respectively (Fig. 8h). All of the indexed habit planes are given in Table 3. Recall that these indexations are obtained by tilting the habit planes edge-on and verifying that the reconstruction projections are fully compatible with the tilt-series micrographs. When there are too many differences between the tilt-series and the tomographic reconstruction, these loops are not kept for further analyses. Through the full tilt-series, 24 habit planes of dislocation loops remained with precise indexation.

Dislocation interactions with loops can also be seen. DET is an ideal tool for analyzing dislocation interactions, as it makes it possible to have access to orientations that facilitate the microstructure deciphering [24,42–44]. Fig. 9 shows an interaction between a dislocation segment with a $\pm 1/3[\bar{2}110]$ Burgers vector and two $\pm 1/3[1\bar{2}10]$ loops whose habit planes are $(1\bar{2}10)$, i.e. two pure edge loops. The Burgers vector of this junction is the combination of $\pm 1/3[1\bar{2}10]$ and $\pm 1/3[\bar{2}110]$, i.e. $\pm 1/3[\bar{1}\bar{1}20]$. This junction is not visible in the 3D reconstruction, because the tilt-series was acquired with the $1\bar{1}00$ diffraction vector where dislocations with $\pm 1/3[\bar{1}\bar{1}20]$ Burgers vectors are not in contrast.

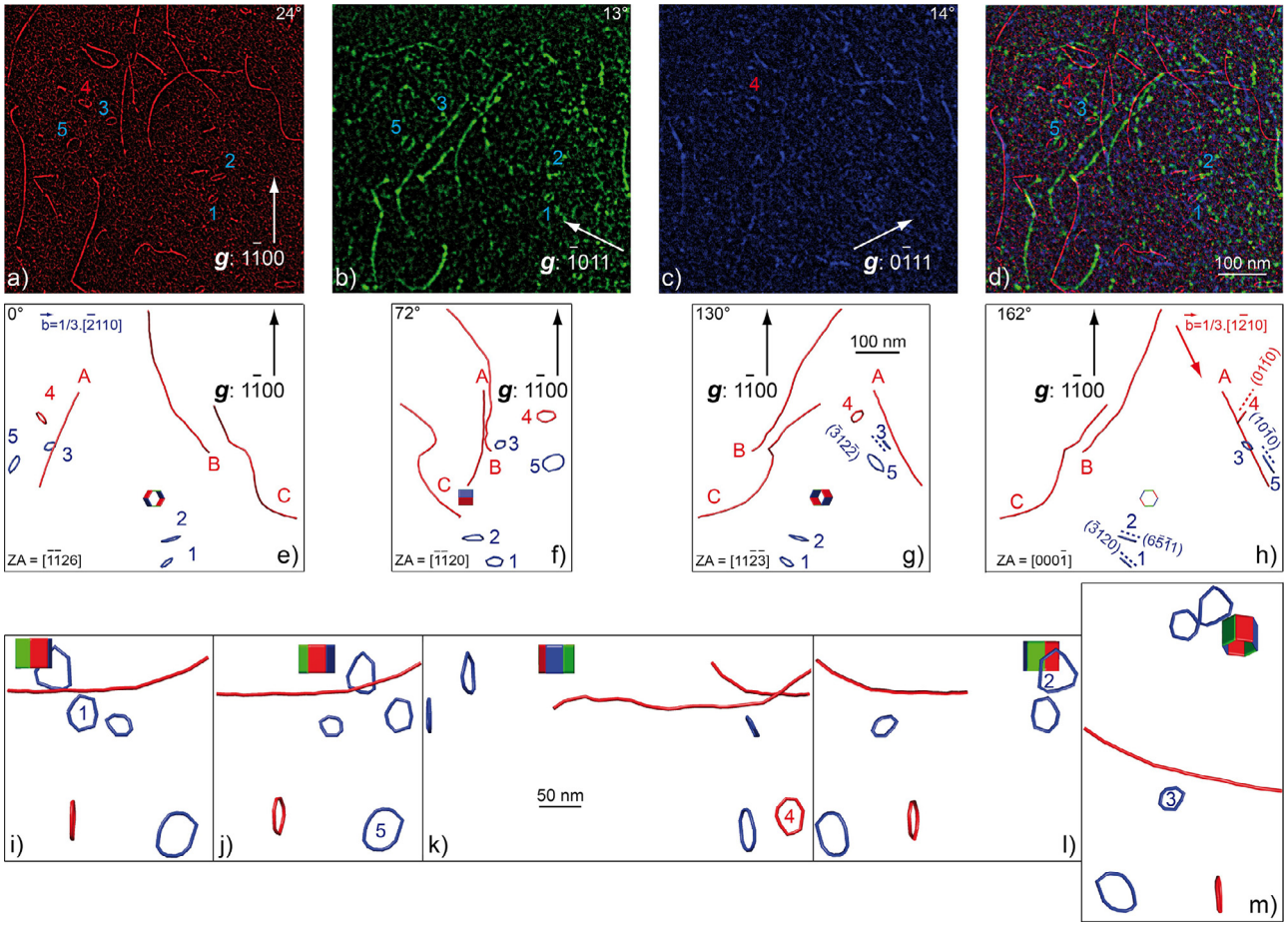

Fig. 8. Dislocation loop characterizations of the irradiated Zr specimen: (a) micrograph in WBDF-STEM mode obtained with g: $1\bar{1}00$, dislocations with $\pm1/3[1\bar{2}10]$ and $\pm1/3[\bar{2}110]$ Burgers vectors are in contrast. Loops with $\pm1/3[1\bar{2}10]$ or $\pm1/3[\bar{2}110]$ Burgers vectors are shown respectively by red or blue numbers; (b) micrograph in WBDF-TEM mode obtained with g: $\bar{1}011$, dislocations with $\pm1/3[\bar{2}110]$ and $\pm1/3[11\bar{2}0]$ Burgers vectors are in contrast (loops are pointed out by blue numbers); (c) micrograph in WBDF-TEM mode obtained with g: $0\bar{1}11$, dislocations with $\pm1/3[1\bar{2}10]$ and $\pm1/3[11\bar{2}0]$ Burgers vectors are in contrast (the loop is pointed out by the red number 4); (d) 3 previous micrograph superimposition to facilitate Burgers vector indexations; (e) tomographic reconstruction projection along $[\bar{1}\bar{1}26]$ (5 loops have been reconstructed); (f) projection along $[\bar{1}\bar{1}20]$; (g) projection along $[11\bar{2}\bar{3}]$ (the $(\bar{3}11\bar{2})$ habit plane of loop n°3 is edge-on); (h) projection along $[000\bar{1}]$ (the habit planes of loops n°1, 2, 4 and 5 are edge-on, they are $(\bar{3}120)$, $(65\bar{1}1)$, $(01\bar{1}0)$ and $(10\bar{1}0)$ respectively); (i–m) projections where the normal of the loop habit planes 1, 5, 4, 2 and 3 are edge-on respectively. It is worth noticing that the spatial resolution of the WBDF-STEM micrograph is higher than the WBF-TEM ones. A slight ellipticity along [0001], notably for loops n°1, 4 and 5, can be also noticed. The movie version of redrawn volume of these loops is shown in Supplemental file S7. (For interpretation of the references to color in this figure legend, the reader is referred to the web version of this article.).

Table 3
Indexation of habit planes of the 24 dislocation loops analyzed in the irradiated Zr specimen.

Habit plane for loops having $\pm1/3[1\bar{2}10]$ Burgers vector	Angle between the normal of habit plane and the Burgers vectors	Habit plane for loops $\pm1/3[\bar{2}110]$ Burgers vector	Angle between the normal of habit plane and the Burgers vectors
2 loops in $(01\bar{1}0)$	30	4 loops in $(10\bar{1}0)$	30
1 loop in $(1\bar{3}21)$	16	1 loop in $(\bar{2}110)$	0
1 loop in $(1\bar{4}30)$	16	1 loop in $(\bar{3}120)$	11
2 loops in $(1\bar{5}40)$	19	1 loop in $(6\bar{4}\bar{2}1)$	12
2 loops in $(1\bar{5}42)$	23	2 loops in $(\bar{4}310)$	16
1 loop in $(02\bar{2}1)$	33	1 loop in $(8\bar{6}\bar{2}1)$	17
1 loop in $(2\bar{3}1\bar{4})$	41	1 loop in $(4\bar{1}\bar{3}1)$	18
		1 loop in $(65\bar{1}1)$	22
		1 loop in $(4\bar{1}\bar{3}2)$	23
		1 loop in $(3\bar{1}\bar{2}2)$	25

5. Discussion

5.1. Dislocation glide at room temperature in recrystallized Zircaloy-4

The tomographic analysis performed after straining at room temperature shows primarily screw dislocations (18 of 29 dislocations). When non-screw segments are seen, the glide plane has been analysed (11 dislocations). In one of the eleven cases, the dislocation line was clearly in the first order pyramidal slip. In ten of the eleven cases, prismatic slip was determined. For three of these ten dislocations, it was noticed that part of the dislocation was also lying in the first order pyramidal plane, indicating that the dislocation had partially cross-slipped from the prismatic plane to the pyramidal plane. No dislocation line was seen in the basal plane.

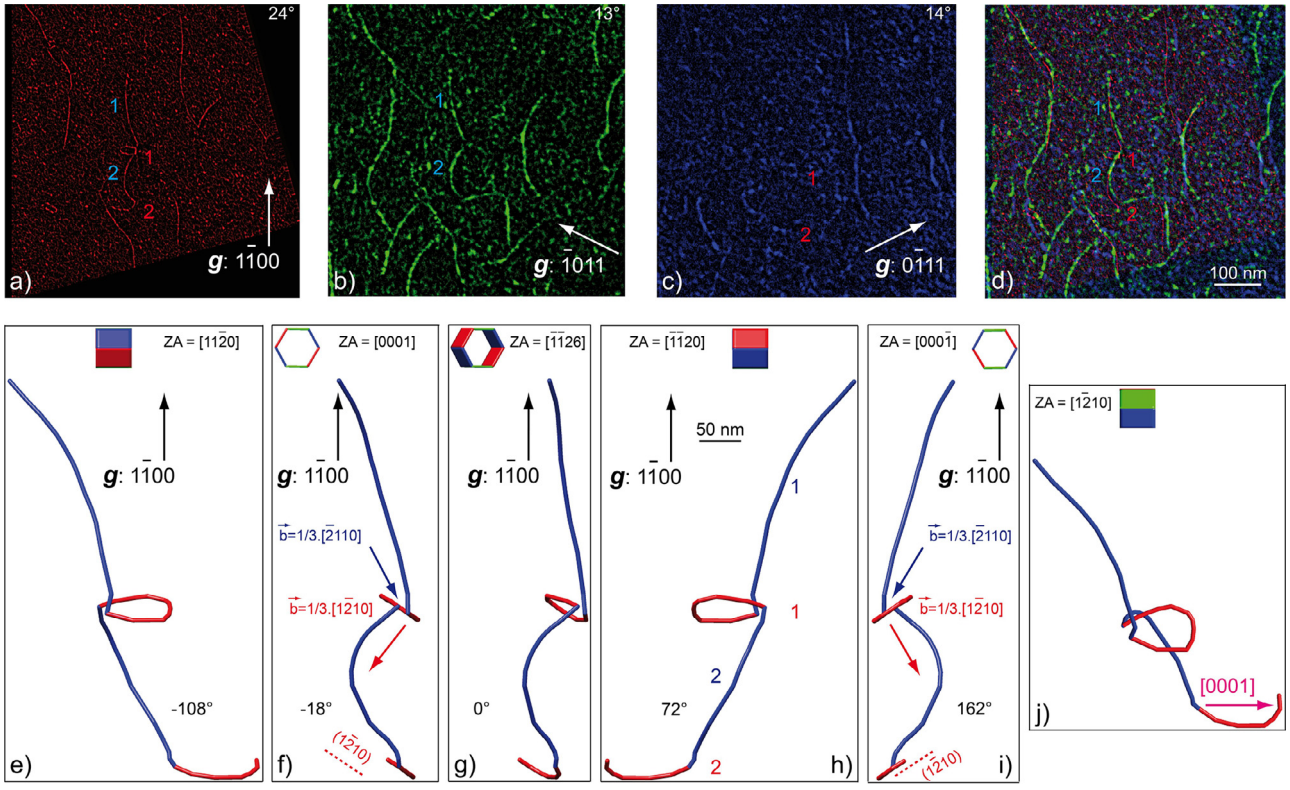

Fig. 9. Double interaction between a dislocation segment and 2 dislocation loops of the irradiated Zr specimen: (a) micrograph in WBDF-STEM mode obtained with *g*: 1$\bar{1}$00, the dislocation segment (±1/3[$\bar{2}$110] Burgers vector) and the dislocation loops (±1/3[1$\bar{2}$10] Burgers vector) are in contrast and pointed out by blue and red numbers respectively; (b) micrograph in WBDF-TEM mode obtained with *g*: $\bar{1}$011, both loops are out of contrast; (c) micrograph in WBDF-TEM mode obtained with *g*: 0$\bar{1}$11, both loops are in contrast (with a bad contrast quality); (d) 3 previous micrographs superimposition to facilitate Burgers vector indexations; (e) tomographic reconstruction projection along [11$\bar{2}$0]; (f) projection along [0001] (the (1$\bar{2}$10) habit planes of the loops in interaction with the dislocation segment are edge-on; both loops are in pure climb configurations); (g) projection along [$\bar{1}\bar{1}$26], *i.e.* the foil surface normal; (h) projection along [$\bar{1}\bar{1}$20]; (i) projection along [000$\bar{1}$]; (j) projection along the normal of the loop habit plane. It is worth noting a high ellipticity along [0001]. The movie version of redrawn volume of these two interactions is shown in Supplemental file S8. (For interpretation of the references to color in this figure legend, the reader is referred to the web version of this article.).

It is known that zirconium deforms easily by glide of dislocations in the prismatic planes of the hcp lattice. In the case of pure zirconium, it was shown by Clouet et al. [45], using ab-initio simulations and in-situ straining experiments, that there is no significant lattice friction during the glide of dislocations in the prismatic planes. However, in the case of Zr-O alloys [46], dislocation glide in prismatic planes is governed by the interaction between oxygen atoms and screw dislocations, which promotes short range double cross-slip from the prismatic plane to the first order pyramidal plane and then back to the prismatic plane. This process creates atomic jogs on the screw dislocation, leading to an apparent lattice friction acting against screw dislocation motion in zirconium alloys containing oxygen. Because the velocity of screw segments is lower than that of edge segments, the microstructure is mainly composed of long screw dislocations, which is why nearly all of the dislocations observed after straining are of screw character (or close to screw character).

The observation of short <a> dislocation segments that have cross-slipped into the first order pyramidal plane is consistent with the analysis proposed by Chaari et al. [46] based on atomistic computations.

5.2. Dislocation loop formation under irradiation

Under irradiation, point defects (interstitials and vacancies) are created. They diffuse and cluster together to create point defect clusters in the form of small disks made either of vacancies or interstitial atoms. These disks are called prismatic dislocation loops because a dislocation line surrounds the disk of point defects, and the Burgers vector does not belong to the habit plane of the loop. In the case of zirconium, the literature indicates that most of the dislocation loops have an <a> Burgers vector and are located close to the prismatic planes [47–49]. In order to confirm these early studies, dislocation electron tomography was used to analyse the loop habit planes. As explained earlier, for some loops, the projection of the reconstructed volume was not in correct agreement with the images. Therefore, only 24 loops were kept for this analysis. For these 24 loops, the Burgers vector was also analysed using the extinction method. The normal to the loop habit plane, depending on its Burgers vector, for these 24 loops is plotted in Fig. 10. The loop normal directions are also represented in a standard triangle. From these figures, it can be seen that for only one loop, the normal of the loop habit plane is parallel to its Burgers vector. This shows that except for one of the 24 cases, the loops are not pure edge; that is, the normal of the habit plane is not parallel to the Burgers vector. The normal to the loop habit plane is tilted up to 33° away from its Burgers vector and even up 41° in the case of one loop (see Table 3). It was found that most of the normals to the loop habit planes lie around the direction ⟨10$\bar{1}$0⟩, which is in good agreement with early results obtained on neutron irradiated samples [47–49]. They are tilted in the basal plane up to 20° of the direction ⟨10$\bar{1}$0⟩ and are often tilted away, up to 20° toward the [0001] direction. Only three loops do not exhibit this overall trend. Except for these three loops, the normals to the habit planes of all 21 loops lie in the surface shown in Fig. 10(b). In Fig. 11, the experimental results given in [47,48] are reported,

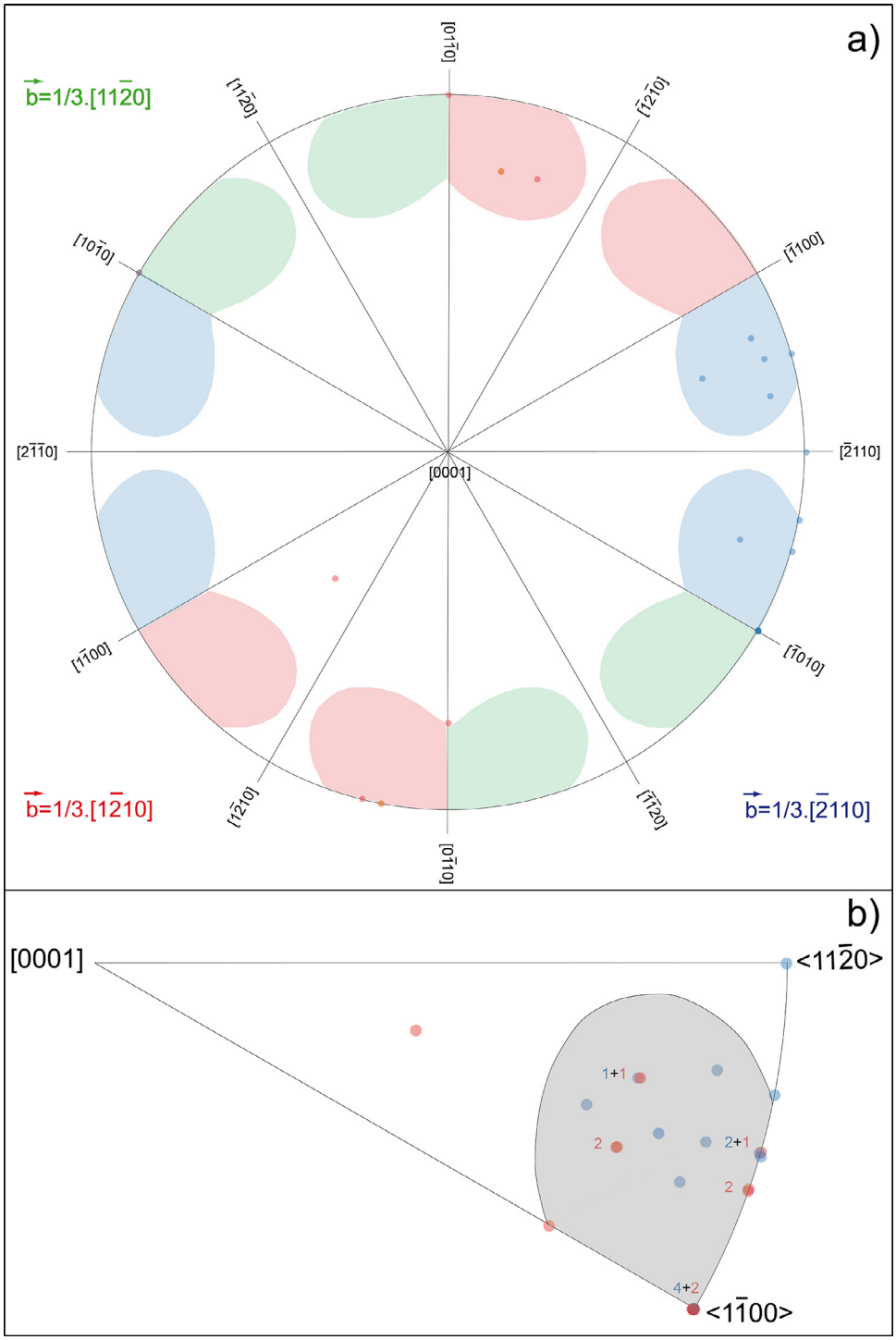

Fig. 10. Habit planes of the dislocation loops: (a) stereographic projection along the [0001] direction of loop plane normal positions (the vast majority of the directions are situated on the "butterfly-wings" distribution of the stereographic projection [48] for both red and blue loops; (b) gathering of data in a single triangle of the stereographic projection (red and blue numbers count the superimposition projections). (For interpretation of the references to color in this figure legend, the reader is referred to the web version of this article.).

showing the good agreement with the new results obtained using DET.

According to Kelly and Blake [48], who referred to the work of Bacon and Crocker [50], perfect <a> loops, that are able to tilt on their cylinder, are not pure edge because of the minimization of line energy. Because a screw dislocation has a lower line energy per unit length than an edge dislocation, the rotation of the loop plane normal away from the pure edge orientation should be energetically favourable, at least to a certain extent, because the line length increases during the tilting. Using Wolfer's [51] calculations, Dai et al. [52] provided an analytical model for the dislocation loop self-energy. From this calculation, it was shown that the most stable <a> loops lie close to the {11$\bar{2}$0} planes (pure edge loop), which is not what is observed experimentally. This suggests that the explanation given by Kelly and Blake, concerning the decrease of the total energy when the loop deviates from its pure

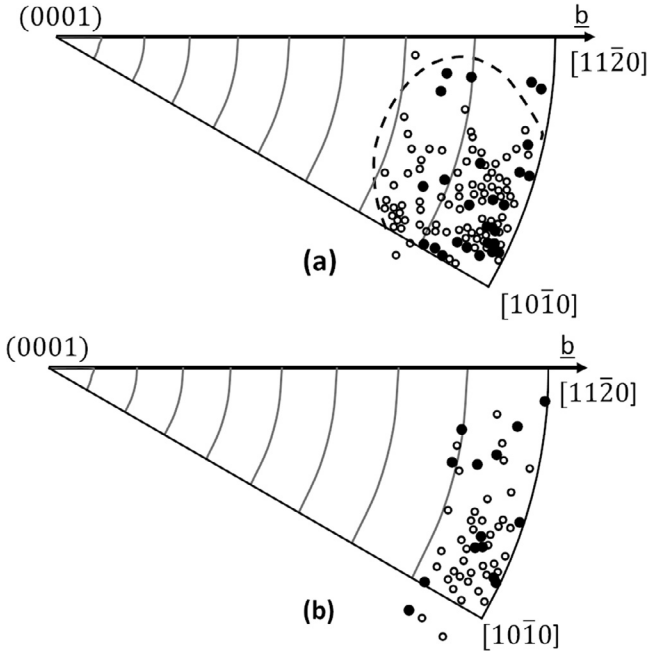

Fig. 11. Loop plane normal represented in a single triangle of the stereographic projection considering that the Burgers vector is 1/3[11$\bar{2}$0]. (a) Zirconium irradiated by neutrons up to 1.4 × 10^{24} n.m^{-2}, from Kelly and Blake [48]. (b) Zone-refined zirconium irradiated by neutrons at 395°C up to 6.4 × 10^{23} n.m^{-2}, from Jostsons et al. [47]. Vacancy loops are represented by open circles and interstitial loops by full circles.

edge character, is not valid. Instead, Dai et al. have suggested that this may be the result of the elastic anisotropy of zirconium, which was not considered in Wolfer's model.

In order to investigate this phenomenon in more detail, Dai et al. [52] performed MD simulations. They studied interstitial <a> loops equilibrated at four different temperatures and showed that <a> interstitial loops are not pure edge but lie in between the {10$\bar{1}$0} and {11$\bar{2}$0} planes with a small tilt toward the basal plane. These simulation results are thus in correct agreement with early experimental results using conventional TEM analysis and also with our results using dislocation electron tomography. It is worth pointing out that when square loops are modelled using MD simulations, as was done by Serra and Bacon [53], the loops are pure edge, suggesting a possible role of the shape of the loop on its stable habit plane. Further modelling work is thus needed to better understand the origin of the deviation from the pure edge character of <a> dislocation loops in zirconium.

5.3. Dislocation climb under irradiation: helical dislocations

Whereas before irradiation the linear dislocations were mainly of screw character, after irradiation, the dislocations no longer exhibited any screw character. Only very small screw segments along the dislocation lines were found (blue and red segments shown in Fig. 7). The dislocations exhibited a mixed character all along the dislocation line. The dislocations were wavy in three dimensions, and no glide plane could be found for the entire dislocation line since the segments along the dislocation line do not belong to the same plane. This proves that the dislocations have moved under irradiation by climb, because of the differential absorption of point defects.

In order to evaluate the magnitude of dislocation climb under ion irradiation at 450°C, a part of the reconstructed volume was observed along the [$\bar{1}$2$\bar{1}$0] and [$\bar{2}$110] zone axes (Fig. 12). It can be seen in Fig. 12a (zone axis [$\bar{1}$2$\bar{1}$0]) that two red dislocations can be encompassed into cylinders with diameters (d) 165 and 275 nm respectively. In Fig. 12b (zone axis [$\bar{2}$110]), two blue dislocations are encompassed into cylinders with diameters (d) 185 and 210 nm respectively. When tilting the reconstructed volume with zone axis [08$\bar{8}$5] (projection of the reconstructed volume along the [08$\bar{8}$5] direction, this direction being perpendicular to the [$\bar{2}$110] direction), we can notice that the two blue dislocations tend to follow a helical shape with a period (helix pitch or turn separation λ) of approximately 400 nm in this orientation condition. Concerning the two red dislocations, when the reconstructed volume is projected along the [10$\bar{1}$0] direction (the [1$\bar{2}$10] Burgers vector is perpendicular to the [10$\bar{1}$0] direction), we can guess that the two red dislocations follow a helical shape with periods of approximately 435 and 460 nm in this orientation condition. From this measurement, it is possible to compute the angle θ between the dislocation line and the Burgers vector, which corresponds to the axis of the helix, as $\tan(\theta) = d/(\lambda/2)$. The two red dislocation θ angles are 37° and 50° respectively, and the two blue dislocation θ angles are 43° and 46° respectively (see Table 4).

Table 4
Geometrical parameters of helical dislocations.

	Red 1	Red 2	Blue 4	Blue 5
d	275 nm	165 nm	210 nm	185 nm
λ	460 nm	435 nm	400 nm	400 nm
θ	50°	37°	46°	43°

It is interesting to compare our observations with a previous study that we performed using electron irradiation on the same alloy [21] at 450°C. In this previous work, we obtained a regular shape for a helical dislocation, but the diameter of the encompassing cylinder (d) was only 20 nm. In this previous work, we also analysed the helix pitch (λ), which was around 40 nm after a dose of 0.06 dpa under electron irradiation. The angle θ was also computed and was found to evolve under irradiation until reaching a value between 45° and 50°. It is interesting to note that although the geometries of the helix are different between ion irradiation and electron irradiation, the angles θ measured are similar.

From the literature, it appears that the shape of the helix strongly depends on the material studied and how the helix is created. In the case of a Cu-Zn-Al-Ni alloy quenched in the β phase [54], the helix periodicity (λ) was found to be 160 nm and the helix diameter (d) was 260 nm, leading to an angle θ equal to 73°. In the case of neutron irradiated Fe-9Cr alloy, the helix periodicity (λ) was found to be 66.7 nm and the helix diameter (d) was 72.5 nm, leading to an angle θ equal to 65°.

The formation of helical dislocations is the result of the climb of initially nearly screw dislocations because of the absorption of point defects. In the case of quenched metals, there is a supersaturation of vacancies. This supersaturation of vacancies creates a chemical force on the dislocation, leading to its climb by absorption of vacancies. Under irradiation, the situation is more complex since there is both a supersaturation of vacancies and a supersaturation of self-interstitial atoms. In that case, the climb of dislocations results from the differential absorption of interstitials versus vacancies depending on the other sinks present in the material.

Several authors [55–58] have studied theoretically helical dislocations, especially in the case of quenched metals. Weertman [58] showed that the equilibrium form of a dislocation is a helix, when there is a chemical force resulting from a vacancy supersaturation. The equilibrium shapes of helical dislocations are governed by the amount of vacancies absorbed by dislocations during their climb, by the repulsive interaction between helical arms, and by dislocation line tension energies. Since dislocations are able to glide on their cylinders, they can freely adjust their shapes. De

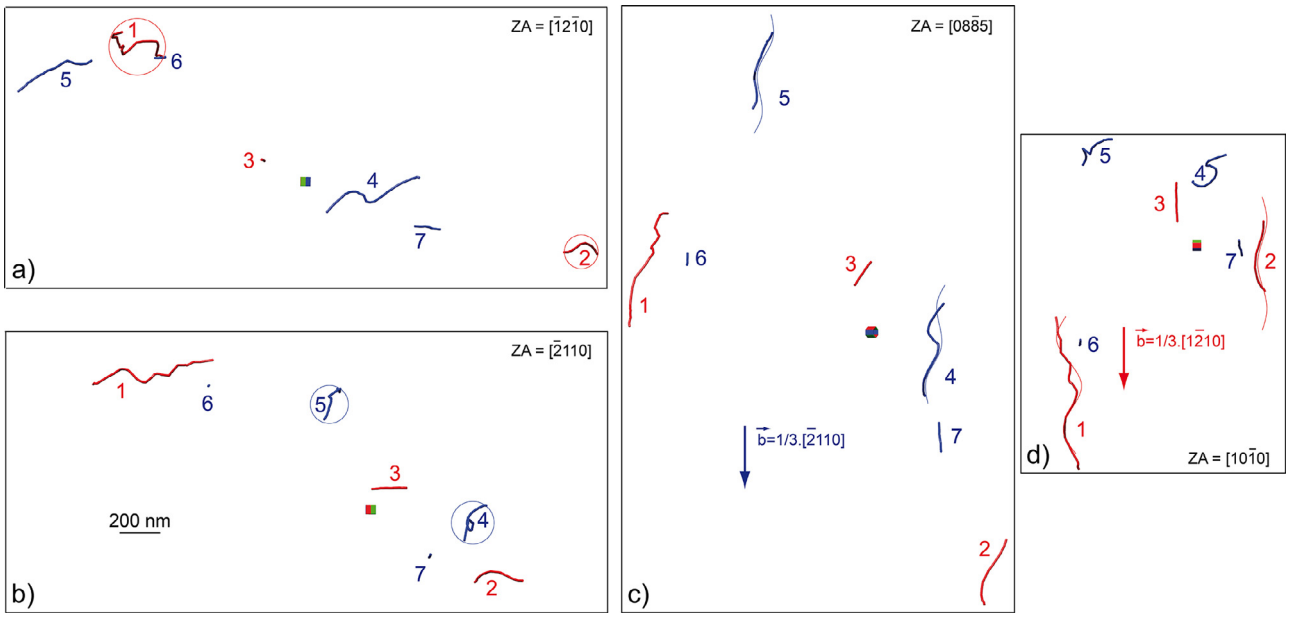

Fig. 12. Helix loop size evaluation: (a) tomographic reconstruction projection along [1$\bar{2}$10], a red screw dislocation (labelled 3) is edge-on and 2 red dislocations (labelled 1 and 2) are not so far from screw nature; (b) projection along [$\bar{2}$110], 2 blue screw dislocations (labelled 6 and 7) are edge-on and 2 blue dislocations (labelled 4 and 5) are not so far from screw nature; (c) projection along [08$\bar{8}$5] (the ±1/3[$\bar{2}$110] Burgers vector is perpendicular to the [08$\bar{8}$5] direction), we can make an estimation of the blue helical pitch; (d) projection along [10$\bar{1}$0] (the ±1/3[1$\bar{2}$10] Burgers vector is perpendicular to the [10$\bar{1}$0] direction), we can make an estimation of the red helical pitch. (For interpretation of the references to color in this figure legend, the reader is referred to the web version of this article.).

Wit [55] showed that for a given amount of absorbed vacancies and for a given length of the helix cylinder (fixed end-points), the most stable helices are those with only one turn, and the largest diameter, which is not what is observed experimentally.

De Wit [55], Friedel [57] and Grilhé [56] also showed that for a given amount of absorbed vacancies and for a given number of turns, but for an adjustable cylinder length (not fixed end-points), there is an equilibrium configuration: a tightly wound helix will try to extend itself, while a nearly straight helix will try to compress itself, resulting in intermediate θ angles at equilibrium. Grilhé [56] showed that the ratio between the pitch of the helix and the diameter of the helix is equal to 1.5 at equilibrium, which leads to an angle θ equal to 53°. Our experimental observations are thus in correct agreement with this theoretical model.

Recently, Liu et al. [59] used a coupled glide-climb model in 3D discrete dislocation dynamics to reproduce the formation of a helix with multiple turns. The origin of the formation of multiple turns, which is considered theoretically to be unstable under static conditions, is related to the dynamical evolution of the system. Haley et al. [60], using similar simulation tools, also managed to obtain a stable helix with multiple turns under vacancy supersaturation. The simulated period (λ) was equal to 75 nm and the helix diameter (d) was 79.2 nm, leading to an angle θ equal to 65°.

5.4. Interactions between dislocations and loops

The tomographic analysis has been able to reveal the 3D geometry of an interaction between a dislocation and a loop. It is known that when an <a> dislocation glides, it can interact with <a> loops via various possible mechanisms. If the dislocation and the loop have parallel Burgers vectors, the loop can be incorporated into the dislocation as a helical turn. If the dislocation and loop have different Burgers vectors (say $\underline{a}_1$ and $\underline{a}_2$), a reaction can occur leading to the formation of a junction with Burgers vector $-\underline{a}_3$. This reaction is energetically favorable since $\|\underline{a}_3\| < \|\underline{a}_1\| + \|\underline{a}_2\|$. These types of reactions have been recently simulated using MD and 3D Discrete Dislocation Dynamics, by considering a dislocation gliding and interacting with various types of loops [53,61–65].

The tomographic analysis performed in our experiments has proven that dislocations climb. The configuration observed in Fig. 9 is thus the result of the interaction between a climbing dislocation and a loop. It has also been shown, using extinction techniques, that the Burgers vector of the loop (±1/3[1$\bar{2}$10]) is different from the Burgers vector of the dislocation (±1/3[$\bar{2}$110]). A junction (with Burgers vector ±1/3[$\bar{1}\bar{1}$20]) is thus created, but it is invisible in our observations. The pure climb plane of an edge dislocation with Burgers vector ±1/3[$\bar{2}$110] is the plane ($\bar{2}$110). As a consequence, the dislocation and the junction do not have the same climb planes, and the junction therefore acts as a pinning point against dislocation climb, as for glide.

5.5. Implications on in-reactor deformation of zirconium alloys

This three-dimensional transmission electron tomographic analysis of the dislocation microstructure of an irradiated pre-deformed Zircaloy-4 specimen shows that dislocation climb occurs in zirconium alloys under ion irradiation conducted at 450°C. This process of dislocation climb under irradiation, studied here in the absence of any applied stress, is an important mechanism during the in-reactor deformation of zirconium alloys under low applied stress [2,66].

Furthermore, these tomographic observations show interactions between loops and dislocations during their climb. The resulting interactions create pinning points for dislocations that make their climb more difficult. Because irradiation damage progressively builds up under irradiation, until reaching a steady state, the density of pinning points also progressively increases under irradiation until reaching a steady state. This phenomenon could explain the progressive transition from primary irradiation creep to secondary irradiation creep observed in reactor [2,66].

To better assess these mechanisms, similar experiments will be performed on samples subjected to simultaneous irradiation and applied stress, which will be the subject of future studies.

6. Conclusion

DET is a unique tool for investigating the 3D geometry of dislocations and can provide details of the deformation processes at the nano-scale. This technique was used to study zirconium alloys and has been able to prove that after straining at room temperature, non-irradiated recrystallized Zircaloy-4 exhibited mainly screw dislocations with <a> Burgers vectors. When non-screw segments were observed, it was shown that dislocations had glided primarily in the prismatic planes and also, but to a lesser extent, in the first order pyramidal planes.

Concerning recrystallized Zircaloy-4 that had been pre-strained at room temperature and then irradiated with Zr ions at 450°C, the habit plane of dislocation loops created under irradiation was analysed accurately using DET. It was found that most of the loops were not pure edge. Their habit planes were located around the $\{10\bar{1}0\}$ family planes, tilted up to 20° towards the (0001) plane and up to 20° towards the $\{11\bar{2}0\}$ family planes. This result is in good agreement with the early works done using conventional TEM on neutron-irradiated samples.

DET has been able to prove that the dislocations created during prior straining evolved under irradiation. It was shown that they were no longer screw dislocations. They exhibited complex 3D shapes proving that dislocation climb occurred under irradiation. For some dislocations, shapes similar to a helix were observed. This structure is the result of the climb of a nearly screw dislocation under supersaturation of point defects.

Finally, using DET, the details of an interaction between a dislocation and two loops were analysed. This interaction probably occurred during dislocation climb, resulting in the pinning of the dislocation. These observations performed using DET provide an interesting insight into the deformation processes occurring under irradiation, illustrating two antagonistic phenomena: dislocations climb under irradiation, resulting in strain, and these dislocations are also pinned by loops created under irradiation, thus impeding further climb and glide.

Data and materials availability

All raw data are available at https://zenodo.org/record/4508831.

CRediT Authorship contribution statement

Alexandre Mussi and **Fabien Onimus** developed the study. **Fabien Onimus** prepared the specimens and the thin foils. **Alexandre Mussi** and **Ahmed Addad** conducted the TEM characterizations. **Alexandre Mussi** and **Fabien Onimus** wrote the paper.

Declaration of Competing Interest

The authors declare that they have no known competing financial interests or personal relationships that could have appeared to influence the work reported in this paper.

Acknowledgment

The TEM national facility in Lille (France) is supported by the Conseil Regional du Nord-Pas de Calais, the European Regional Development Fund (ERDF), and the Institut National des Sciences de l'Univers (INSU, CNRS). This project has received funding from the European Research Council (ERC) under the European Union's Horizon 2020 research and innovation program under grant agreement 787198 – TimeMan.

This work is also funded by the French Tripartite Institute (CEA-EDF-Framatome) through the GAINE project. The authors also want to thank Matthew Bono (CEA) for linguistic proofreading.

Supplementary materials

Supplementary material associated with this article can be found, in the online version, at doi:10.1016/j.actamat.2021.116964.

References

[1] D.G. Franklin, R.B. Adamson, Implications of Zircaloy creep and growth to light water reactor performance, J. Nucl. Mater. 159 (1988) 12–21 Oct., doi:10.1016/0022-3115(88)90082-7.
[2] R.A. Holt, In-reactor deformation of cold-worked Zr–2.5Nb pressure tubes, J. Nucl. Mater. 372 (2–3) (2008) 182–214 Jan., doi:10.1016/j.jnucmat.2007.02.017.
[3] R.B. Adamson, C.E. Coleman, M. Griffiths, Irradiation creep and growth of zirconium alloys: a critical review, J. Nucl. Mater. 521 (2019) 167–244 Aug., doi:10.1016/j.jnucmat.2019.04.021.
[4] F. Onimus, S. Doriot, J.-L. Béchade, Radiation effects in zirconium alloys, Compr. Nucl. Mater. (2020) 1–56, doi:10.1016/b978-0-12-803581-8.11759-x.
[5] F. Onimus, T. Jourdan, C. Xu, A.A. Campbell, M. Griffiths, Irradiation creep in materials, Compr. Nucl. Mater. (2020) 310–366, doi:10.1016/b978-0-12-803581-8.11645-5.
[6] V. Fidleris, The irradiation creep and growth phenomena, J. Nucl. Mater. 159 (1988) 22–42 Oct., doi:10.1016/0022-3115(88)90083-9.
[7] D.G. Franklin, G.E. Lucas, A.L. Bement, Creep of Zirconium Alloys in Nuclear Reactors, ASTM STP 815, ASTM International, 1983.
[8] A. Rogerson, Irradiation growth in zirconium and its alloys, J. Nucl. Mater. 159 (1988) 43–61 Oct., doi:10.1016/0022-3115(88)90084-0.
[9] J.R. Matthews, M.W. Finnis, Irradiation creep models — an overview, J. Nucl. Mater. 159 (1988) 257–285 Oct., doi:10.1016/0022-3115(88)90097-9.
[10] J. Gittus, Creep, Viscoelasticity and Creep Fracture in Solids, Elseviers Applied Science Publishers, London, 1975.
[11] J.H. Gittus, Theory of dislocation-creep due to the frenkel defects or interstitialcies produced by bombardment with energetic particles, Philos. Mag. 25 (2) (1972) 345–354 Feb., doi:10.1080/14786437208226809.
[12] F. Nichols, Mechanistic modeling of Zircaloy deformation and fracture in fuel element analysis, Zircon. Nucl. Ind. Seventh Int. Symp. ASTM STP 939 (1987) 5–22.
[13] F.A. Nichols, Theory of the creep of zircaloy during neutron irradiation, J. Nucl. Mater. 30 (3) (1969) 249–270 Apr., doi:10.1016/0022-3115(69)90241-4.
[14] R. Bullough, J.R. Willis, The stress-induced point defect-dislocation interaction and its relevance to irradiation creep, Philos. Mag. 31 (4) (1975) 855–861 Apr., doi:10.1080/14786437508229635.
[15] P.T. Heald, M.V. Speight, Steady-state irradiation creep, Philos. Mag. 29 (5) (1974) 1075–1080 May, doi:10.1080/14786437408226592.
[16] W.G. Wolfer, M. Ashkin, Diffusion of vacancies and interstitials to edge dislocations, J. Appl. Phys. 47 (3) (1976) 791–800 Mar., doi:10.1063/1.322710.
[17] C.H. Woo, Irradiation creep due to elastodiffusion, J. Nucl. Mater. 120 (1) (1984) 55–64 Feb., doi:10.1016/0022-3115(84)90170-3.
[18] G.J.C. Carpenter, J.F. Watters, Vacancy precipitation in zirconium alloys, Acta Metall. 21 (9) (1973) 1207–1214 Sep., doi:10.1016/0001-6160(73)90161-2.
[19] S.N. Buckley, S.A. Manthorpe, Dislocation loop nucleation and growth in zirconium-2.5 wt% niobium alloy during 1 MeV electron irradiation, J. Nucl. Mater. 90 (1–3) (1980) 169–174 May, doi:10.1016/0022-3115(80)90254-8.
[20] M. Griffiths, M.H. Loretto, R.E. Smallman, Electron damage in zirconium - II, J. Nucl. Mater. 115 (2–3) (1983) 313–322 Apr., doi:10.1016/0022-3115(83)90322-7.
[21] M. Gaumé, F. Onimus, L. Dupuy, O. Tissot, C. Bachelet, F. Mompiou, Microstructure evolution of recrystallized Zircaloy-4 under charged particles irradiation, J. Nucl. Mater. 495 (2017) 516–528 Nov., doi:10.1016/j.jnucmat.2017.09.004.
[22] J.S. Barnard, High-resolution three-dimensional imaging of dislocations, Science 313 (5785) (2006) 319 –319Jul., doi:10.1126/science.1125783.
[23] Z. Feng, et al., TEM-based dislocation tomography: challenges and opportunities, Curr. Opin. Solid State Mater. Sci. 24 (3) (2020) 100833 Jun., doi:10.1016/j.cossms.2020.100833.
[24] G.S. Liu, S.D. House, J. Kacher, M. Tanaka, K. Higashida, I.M. Robertson, Electron tomography of dislocation structures, Mater. Charact. 87 (2014) 1–11 Jan., doi:10.1016/j.matchar.2013.09.016.
[25] F. Long, J. Kacher, Z. Yao, M.R. Daymond, A tomographic TEM study of tension–compression asymmetry response of pyramidal dislocations in a deformed Zr-2.5 Nb alloy, Scr. Mater. 153 (2018) 94–98.
[26] Z.Q. Feng, C.W. Lin, T.T. Li, X. Luo, G.L. Wu, X.X. Huang, Electron tomography of dislocations in an Al-Cu-Mg alloy, IOP Conf. Ser. Mater. Sci. Eng. 219 (2017) 012018 Jul., doi:10.1088/1757-899x/219/1/012018.
[27] F. Onimus, L. Dupuy, F. Mompiou, In situ TEM observation of interactions between gliding dislocations and prismatic loops in Zr-ion irradiated zirconium alloys, Prog. Nucl. Energy 57 (2012) 77–85 May, doi:10.1016/j.pnucene.2011.10.005.
[28] R. Tewari, K.V. Mani Krishna, S. Neogy, C. Lemaignan, Zirconium and its alloys: properties and characteristics, Compr. Nucl. Mater. (2020) 284–302, doi:10.1016/b978-0-12-803581-8.11735-7.
[29] R.E. Stoller, M.B. Toloczko, G.S. Was, A.G. Certain, S. Dwaraknath, F.A. Garner, On the use of SRIM for computing radiation damage exposure, Nucl. Instrum. Methods Phys. Res. Sect. B Beam Interact. Mater. At. 310 (2013) 75–80 Sep., doi:10.1016/j.nimb.2013.05.008.

[30] J.F. Ziegler, M.D. Ziegler, J.P. Biersack, SRIM – the stopping and range of ions in matter (2010), Nucl. Instrum. Methods Phys. Res. Sect. B Beam Interact. Mater. At. 268 (11–12) (2010) 1818–1823 Jun., doi:10.1016/j.nimb.2010.02.091.
[31] A. Mussi, P. Cordier, S. Demouchy, B. Hue, Hardening mechanisms in olivine single crystal deformed at 1090°C: an electron tomography study, Philos. Mag. 97 (33) (2017) 3172–3185 Sep., doi:10.1080/14786435.2017.1367858.
[32] P.J. Phillips, M.C. Brandes, M.J. Mills, M. De Graef, Diffraction contrast STEM of dislocations: Imaging and simulations, Ultramicroscopy 111 (9–10) (2011) 1483–1487 Aug., doi:10.1016/j.ultramic.2011.07.001.
[33] P.J. Phillips, M.J. Mills, M. De Graef, Systematic row and zone axis STEM defect image simulations, Philos. Mag. 91 (16) (2011) 2081–2101 Jun., doi:10.1080/14786435.2010.547526.
[34] A. Mussi, P. Cordier, S. Demouchy, C. Vanmansart, Characterization of the glide planes of the [001] screw dislocations in olivine using electron tomography, Phys. Chem. Miner. 41 (7) (2014) 537–545 Mar., doi:10.1007/s00269-014-0665-1.
[35] J.M. Rebled, Ll. Yedra, S. Estradé, J. Portillo, F. Peiró, A new approach for 3D reconstruction from bright field TEM imaging: beam precession assisted electron tomography, Ultramicroscopy 111 (9–10) (2011) 1504–1511 Aug., doi:10.1016/j.ultramic.2011.06.002.
[36] S. Hata, et al., High-angle triple-axis specimen holder for three-dimensional diffraction contrast imaging in transmission electron microscopy, Ultramicroscopy 111 (8) (2011) 1168–1175 Jul., doi:10.1016/j.ultramic.2011.03.021.
[37] G.T. Herman, A.V. Lakshminarayanan, A. Naparstek, Convolution reconstruction techniques for divergent beams, Comput. Biol. Med. 6 (4) (1976) 259–271 Oct., doi:10.1016/0010-4825(76)90065-2.
[38] J. Radon, Über die Bestimmung von Funktionen durch ihre Integralwerte längs gewisser Mannigfaltigkeiten, Comput. Tomogr. (1983) 71–86, doi:10.1090/psapm/027/692055.
[39] C. Messaoudi, T. Boudier, C. Sorzano, S. Marco, TomoJ: tomography software for three-dimensional reconstruction in transmission electron microscopy, BMC Bioinformatics 8 (1) (2007) 288, doi:10.1186/1471-2105-8-288.
[40] E.F. Pettersen, et al., UCSF Chimera?A visualization system for exploratory research and analysis, J. Comput. Chem. 25 (13) (2004) 1605–1612, doi:10.1002/jcc.20084.
[41] A. Mussi, et al., Transmission electron microscopy of dislocations in cementite deformed at high pressure and high temperature, Philos. Mag. 96 (17) (2016) 1773–1789 May, doi:10.1080/14786435.2016.1177670.
[42] J. Kacher, I.M. Robertson, In situ and tomographic analysis of dislocation/grain boundary interactions in α-titanium, Philos. Mag. 94 (8) (2014) 814–829 Jan., doi:10.1080/14786435.2013.868942.
[43] A. Mussi, P. Cordier, S. Demouchy, Characterization of dislocation interactions in olivine using electron tomography, Philos. Mag. 95 (4) (2015) 335–345 Jan., doi:10.1080/14786435.2014.1000996.
[44] A. Mussi, M. Nafi, S. Demouchy, P. Cordier, On the deformation mechanism of olivine single crystals at lithospheric temperatures: an electron tomography study, Eur. J. Mineral. 27 (6) (2015) 707–715 Dec., doi:10.1127/ejm/2015/0027-2481.
[45] E. Clouet, D. Caillard, N. Chaari, F. Onimus, D. Rodney, Dislocation locking versus easy glide in titanium and zirconium, Nat. Mater. 14 (9) (2015) 931–936 Jul., doi:10.1038/nmat4340.
[46] N. Chaari, D. Rodney, E. Clouet, Oxygen - Dislocation interaction in zirconium from first principles, Acta Mater. 132 (2017) 416–424 Jun., doi:10.1016/j.actamat.2017.05.008.
[47] A. Jostsons, P.M. Kelly, R.G. Blake, The nature of dislocation loops in neutron irradiated zirconium, J. Nucl. Mater. 66 (3) (1977) 236–256 May, doi:10.1016/0022-3115(77)90113-1.
[48] P.M. Kelly, R.G. Blake, The characterization of dislocation loops in neutron irradiated zirconium, Philos. Mag. 28 (2) (1973) 415–426 Aug., doi:10.1080/14786437308217463.
[49] D.O. Northwood, et al., Characterization of neutron irradiation damage in zirconium alloys — an international 'round-robin' experiment, J. Nucl. Mater. 79 (2) (1979) 379–394 Feb., doi:10.1016/0022-3115(79)90103-x.
[50] D. Bacon, A. Crocker, The elastic energies of symmetrical dislocation loops, Philos. Mag. 12 (115) (1965) 195–198.
[51] W.G. Wolfer, T. Okita, D.M. Barnett, Motion and rotation of small glissile dislocation loops in stress fields, Phys. Rev. Lett. 92 (8) (2004) Feb., doi:10.1103/physrevlett.92.085507.
[52] C. Dai, L. Balogh, Z. Yao, M.R. Daymond, The habit plane of <a>-type dislocation loops in α-zirconium: an atomistic study, Philos. Mag. 97 (12) (2017) 944–956 Feb., doi:10.1080/14786435.2017.1287441.
[53] A. Serra, D.J. Bacon, Atomic-level computer simulation of the interaction between 1/3<11-20>{1-100} dislocations and 1/3<11-20>interstitial loops in alpha-zirconium, Model. Simul. Mater. Sci. Eng. 21 (4) (2013) 045007 Apr., doi:10.1088/0965-0393/21/4/045007.
[54] G.D. Serrano, J.L. Pelegrina, A.M. Condó, M. Ahlers, Helical dislocations as vacancy sinks in β phase Cu–Zn–Al–Ni alloys, Mater. Sci. Eng. A 433 (1–2) (2006) 149–154 Oct., doi:10.1016/j.msea.2006.06.040.
[55] R. de Wit, Self-energy of a helical dislocation, Phys. Rev. 116 (3) (1959) 592–597 Nov., doi:10.1103/physrev.116.592.
[56] J. Grilhé, Formes d'équilibre des dislocations hélicoïdales, J. Phys. Colloq. 27 (C3) (1966) C3183–C3187 Jul., doi:10.1051/jphyscol:1966323.
[57] J. Friedel, Dislocations, Pergamon, 1964.
[58] J. Weertman, Helical dislocations, Phys. Rev. 107 (5) (1957) 1259–1261 Sep., doi:10.1103/physrev.107.1259.
[59] F. Liu, Z. Liu, P. Lin, Z. Zhuang, Numerical investigations of helical dislocations based on coupled glide-climb model, Int. J. Plast. 92 (2017) 2–18 May, doi:10.1016/j.ijplas.2017.02.015.
[60] J.C. Haley, et al., Helical dislocations: observation of vacancy defect bias of screw dislocations in neutron irradiated Fe-9Cr, SSRN Electron. J. (2019), doi:10.2139/ssrn.3406920.
[61] J. Drouet, L. Dupuy, F. Onimus, F. Mompiou, A direct comparison between in-situ transmission electron microscopy observations and Dislocation Dynamics simulations of interaction between dislocation and irradiation induced loop in a zirconium alloy, Scr. Mater. 119 (2016) 71–75 Jul., doi:10.1016/j.scriptamat.2016.03.029.
[62] J. Drouet, L. Dupuy, F. Onimus, F. Mompiou, S. Perusin, A. Ambard, Dislocation dynamics simulations of interactions between gliding dislocations and radiation induced prismatic loops in zirconium, J. Nucl. Mater. 449 (1–3) (2014) 252–262 Jun., doi:10.1016/j.jnucmat.2013.11.049.
[63] K. Ghavam, R. Gracie, Simulations of reactions between irradiation induced<a>-loops and mixed dislocation lines in zirconium, J. Nucl. Mater. 462 (2015) 126–134 Jul., doi:10.1016/j.jnucmat.2015.03.007.
[64] F. Onimus, L. Dupuy, M. Gaumé, W. Kassem, F. Mompiou, Deformation mechanisms of zirconium alloys after irradiation studied by dislocation dynamics simulations and in situ straining experiments in TEM, ASTM STP 1622, 2020.
[65] R.E. Voskoboynikov, Y.N. Osetsky, D.J. Bacon, Self-interstitial atom clusters as obstacles to glide of edge dislocations in α-zirconium, Mater. Sci. Eng. A 400–401 (2005) 54–58 Jul., doi:10.1016/j.msea.2005.03.056.
[66] A. Soniak, N. L'Hullier, J.-P. Mardon, V. Rebeyrolle, P. Bouffioux, C. Bernaudat, Irradiation creep behavior of Zr-base alloys, Zircon. Nucl. Ind. Thirteen. Int. Symp. ASTM STP 1423 (2002) 837–862, doi:10.1520/stp11419s.